J. Fluid Mech. (2006), *vol.* 546, *pp.* 51–60.
doi:10.1017/S0022112005007408 Printed in the United Kingdom

Analysis of thermal dissipation rates in turbulent Rayleigh–Bénard convection

By OLGA SHISHKINA AND CLAUS WAGNER

DLR – Institute for Aerodynamics and Flow Technology, Bunsenstrasse 10, 37073 Göttingen, Germany

(Received 7 May 2005 and in revised form 29 September 2005)

Direct numerical simulations (DNS) of turbulent Rayleigh–Bénard convection in a wide cylindrical container (aspect ratio $\Gamma = 10$) with a lateral wall have been performed for the first time for the Rayleigh numbers 10^5, 10^6 and 10^7 and Prandtl number $Pr = 0.7$. Evaluating the thermal dissipation rates from the generated DNS data, the formation and development of the thermal plumes and their interaction are highlighted. Two new functions σ and τ are defined to determine quantitatively the role of the turbulent background. Evaluating these functions from the DNS data, it is shown that the turbulent background pushes the thermal plumes back and that its contribution to the volume-averaged thermal dissipation rate increases with the Rayleigh number. Further, it is proven analytically that the ratio of the area-averaged (over the top or the bottom plates) to the volume-averaged thermal dissipation rate is greater than or equal to the Nusselt number for all aspect ratios, and Prandtl and Rayleigh numbers.

1. Introduction

Turbulent Rayleigh–Bénard convection, i.e. the thermally driven fluid motion between a lower heated horizontal plate and an upper cooled plate, has been the subject of many investigations. Reviews on this classical problem have been given by Ahlers (2005), Kadanoff (2001), Ahlers, Grossmann & Lohse (2001) and Siggia (1994).

Numerous experimental studies of Boussinesq Rayleigh–Bénard convection proved the existence of different flow patterns depending on the Rayleigh (Ra) and Prandtl (Pr) numbers and the aspect ratio (Γ) of the considered container. Above but close to the onset of convection ($Ra \approx 1.7 \times 10^3$) the flow patterns consist of straight rolls with certain defects induced by the sidewalls (see for example Ahlers 2005). Further above the onset the spiral–defect chaos evolves for low-Prandtl-number fluids ($Pr \leqslant 1$) as reported by Morris *et al.* (1993). Assenheimer & Steinberg (1996) observed hexagon patterns that occur for Rayleigh numbers around 6.8×10^3. Both types of polygon convection cells – those with rising (l-cells) and those with descending (g-cells) motion in the centre – can coexist with the spirals (see for example Getling 1998). When the Rayleigh number exceeds a value of order 10^4 spoke patterns evolve as reported by Busse (1994) and Clever & Busse (1998). These spokes tend to be nearly stationary for lower Ra close to the onset of this type of convection and appear chaotically when Ra exceeds 10^5. A further increase of Ra tears off unstable spokes to form more independent large-scale flow structures generated in the thermal boundary layers and driven by buoyancy. The thermal plumes play an important role in the moderate-Rayleigh-number regime that begins at $Ra = 10^5$. Close to $Ra = 10^8$ large-scale circulation develops as reported for instance by Qiu & Tong (2001) and

Shishkina & Wagner (2005*a*). According to the experimental investigation by Xi, Lam & Xia (2004) this large-scale motion is initiated by thermal plumes.

Most of the flow characteristics strongly depend on the Rayleigh and Prandtl numbers and the aspect ratio. Studying these dependences, Grossmann & Lohse (2004) analysed the thermal dissipation rate and suggested investigating separately the turbulent background and the thermal boundary layers together with the plumes. Considering the thermal plumes as detached boundary layers, the authors split the volume-averaged thermal dissipation rate into two contributions. The first is the thermal dissipation rate due to the plumes together with the smooth parts of the boundary layers and the second is the thermal dissipation rate of the turbulent background. According to the Grossmann–Lohse ansatz the background part of the thermal dissipation rate must dominate for large Ra. On the other hand, analysing the DNS data obtained for a slender cylindrical container, Verzicco & Camussi (2003) showed that the contribution from the horizontal boundary layers (without plumes) to the volume-averaged thermal dissipation rate also increases with Ra. This observation can be construed as evidence of a decreasing role of the plumes in thermally driven convection for high Rayleigh numbers.

In order to investigate plume properties and to check whether the background part of the thermal dissipation rate takes over for large Ra, Grossmann & Lohse (2004) suggested separating the temperature signals into plume and non-plume parts. Although the plumes are easily seen in experiments and in three-dimensional visualizations of DNS data, quantitatively identifying plumes is non-trivial. Belmonte & Libchaber (1996) used large values of the skewness of the temperature derivative to indicate the plumes. Juliem *et al.* (1999) identified plumes using some threshold of the temperature and the vertical velocity values, while Zhou & Xia (2002) used a threshold of the temperature difference. In Ching *et al.* (2004) the plume velocity was associated with a conditionally averaged velocity. In our plume extraction approach we use local thermal dissipation rates, large values of which are associated with the thermal boundary layers and plumes.

Experimental and numerical investigations of Rayleigh–Bénard convection indicate a strong dependence of flow patterns on the aspect ratio. While large-scale circulation is obtained for a low aspect ratio as documented by Verzicco & Camussi (2003), one obtains a vanishing mean flow for the same Rayleigh number and a high aspect ratio (see Shishkina & Wagner 2005*a*). In this paper we present results of the high-aspect-ratio case $\Gamma = 10$, which is closely related to many astrophysical, geophysical and meteorological problems.

2. Direct numerical simulations

The governing dimensionless equations for the Rayleigh–Bénard problem in the Boussinesq approximation can be written as follows:

$$\boldsymbol{u}_t + \boldsymbol{u}\cdot\nabla\boldsymbol{u} + \nabla p = \Gamma^{-3/2} Ra^{-1/2} Pr^{1/2} \nabla^2 \boldsymbol{u} + T\boldsymbol{z}, \quad \nabla\cdot\boldsymbol{u} = 0, \tag{2.1}$$

$$T_t + \boldsymbol{u}\cdot\nabla T = \Gamma^{-3/2} Ra^{-1/2} Pr^{-1/2} \nabla^2 T, \tag{2.2}$$

with $\boldsymbol{u}$ the velocity vector, T the temperature, $\boldsymbol{u}_t$ and T_t their time derivatives and p the pressure. $Ra = \alpha g H^3 \Delta T/(\kappa\nu)$ denotes the Rayleigh number, $Pr = \nu/\kappa$ the Prandtl number, $\Gamma = D/H$ the aspect ratio with H the height and D the diameter of the cylindrical container. Further, α is the thermal expansion coefficient, g the gravitational acceleration, ΔT the temperature difference between the bottom and the top plates, ν the kinematic viscosity and κ the thermal diffusivity. The dimensionless temperature varies between $+0.5$ at the bottom plate and -0.5 at the top plate.

An adiabatic lateral wall is prescribed by $\partial T/\partial r = 0$. Finally, on the solid walls the velocity field vanishes according to impermeability and no-slip conditions.

In the following analysis we use the results of the DNS which we conducted for turbulent Rayleigh–Bénard convection in a cylindrical container for Rayleigh numbers 10^5, 10^6, 10^7, $Pr = 0.7$ and $\Gamma = 10$. The simulations were performed with the fourth-order-accurate finite volume method developed for solving (2.1), (2.2) in cylindrical coordinates (z, φ, r) on staggered non-equidistant grids. For details on the method, namely the fourth-order discretization, the calculation of the velocity field at the cylinder axis, the hybrid explicit/semi-implicit time stepping and the numerical stability of the method refer to Shishkina & Wagner (2004, 2005*b*).

The computational mesh consists of (110, 512, 192) nodes clustered in the vicinity of the rigid walls. This mesh is fine enough to resolve all relevant turbulent scales, since the mean mesh width $h_{DNS} = \max_i(\Delta z_i\, r_i \Delta\varphi_i\, \Delta r_i)^{1/3}$ is smaller than the mesh width $h(Ra)$ needed to resolve the Kolmogorov scale for all considered Rayleigh numbers. According to Grötzbach (1983), $h(Ra) = \pi\Gamma^{-1} Pr^{1/2}(Nu-1)^{-1/4} Ra^{-1/4}$, where

$$Nu = \Gamma^{1/2} Ra^{1/2} Pr^{1/2} \langle u_z T \rangle_{t,S} - \Gamma^{-1} \left\langle \frac{\partial T}{\partial z} \right\rangle_{t,S} \tag{2.3}$$

is the Nusselt number and $\langle\cdot\rangle_{t,S}$ denotes time and area averaging. In particular, $h(10^5) = 4.37 \times 10^{-2}$, $h(10^6) = 1.98 \times 10^{-2}$ and $h(10^7) = 9.20 \times 10^{-3}$, while $h_{DNS} = 6.54 \times 10^{-3}$.

In figure 1 a perspective view of 20 isotherms in a subdomain reveals the three-dimensional nature of the hot plumes calculated in the DNS for $Ra = 10^5$. The corresponding instantaneous temperature fields in (φ, r)-planes located at half-distance between the plates (figure 2*a*) and close to the heated bottom plate (figure 2*d*) reveal the horizontal extent of hot and cold plumes. Comparing hot coherent structures in figure 2(*a*) with those in figure 2(*b*) and 2(*c*) it is observed that they move apart for high Rayleigh numbers. In figure 2(*d*) the temperature distribution for $Ra = 10^5$ close to the bottom plate reflects large-scale structures with a number of fingers. The temperature fields in figure 2(*e*) and figure 2(*f*) show a reorganization of these large-scale structures. At the same time the number of attached fingers increases with the Rayleigh number.

To provide a quantitative measure for the observations mentioned above, we investigated the azimuthally averaged spectral distribution of the advective heat transport $u_z T$ in the central horizontal cross-section and determined the wavelength of its maximum ($\lambda_{\max}$). The value $\lambda_{\max}$ is associated with the typical size of large coherent flow structures as proposed by Hartlep, Tilgner & Busse (2003). In figure 3 the wavelengths $\lambda_{\max}$ are presented as evaluated from the DNS data for the considered Rayleigh numbers. These wavelengths agree well with those by Fitzjarrald (1976), who performed experiments in rectangular containers.

Statistical averaging of the DNS data was performed for more than 6, 18 and 33 time units for $Ra = 10^5$, 10^6 and 10^7, respectively. Evaluating the Nusselt numbers we obtained $Nu = 4.1$ ($Ra = 10^5$), $Nu = 8.2$ ($Ra = 10^6$) and $Nu = 16.4$ ($Ra = 10^7$). The resulting scaling law $Nu = 0.128 Ra^{0.301}$ is in general agreement with those by Niemela *et al.* (2000) and Wu & Libchaber (1992), who reported $Nu = 0.124 Ra^{0.309}$ for $\Gamma = 0.5$ and $Nu = 0.147 Ra^{0.287}$ for $\Gamma = 6.7$, respectively.

3. Thermal dissipation rate analysis

Following Grossmann & Lohse (2004), who considered the thermal plumes as detached boundary layers, we associate the thermal boundary layers and plumes with

FIGURE 1. Hot plumes visualized with 20 isotherms for $T \in [0, 0.5]$ in a subdomain of width $0.2R$, DNS for $Ra = 10^5$, $Pr = 0.7$, $\Gamma = 10$.

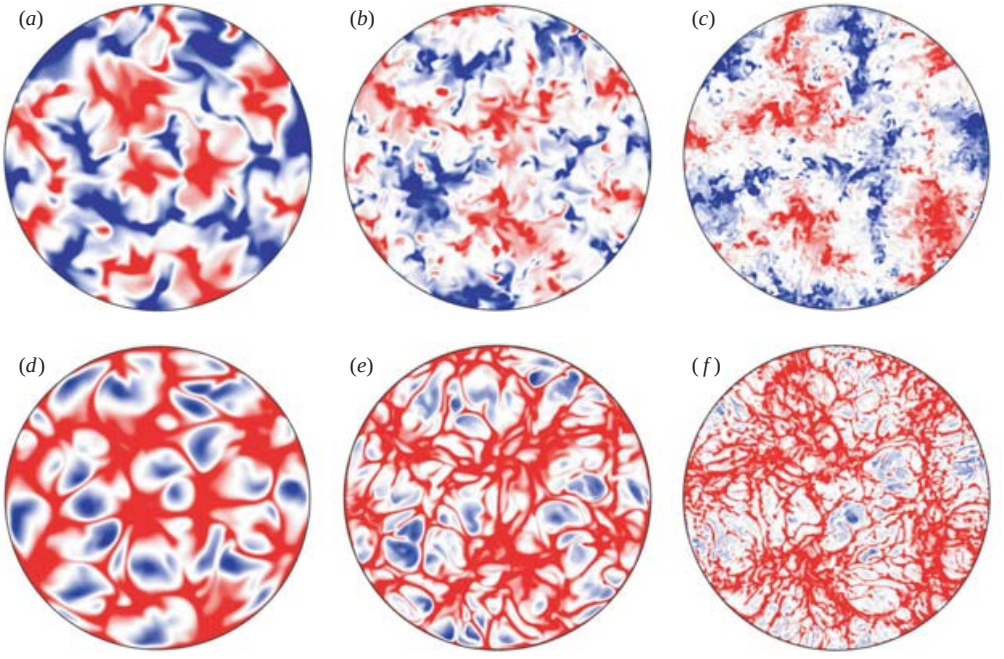

FIGURE 2. Snapshots of the temperature fields $-0.37 \leqslant T \leqslant 0.37$ for $Ra = 10^5$ (a, d) $Ra = 10^6$ (b, e), $Ra = 10^7$ (c, f) in the center cross-section $z = 0.5H$ (a, b, c) and in a plane close to the bottom for $z = H/(2Nu)$ (d, e, f). The colour scale ranges from blue (negative values) through white (zero) to red (positive values).

large values of the thermal dissipation rate

$$\epsilon_\theta = \Gamma^{-3/2} Ra^{-1/2} Pr^{-1/2} (\nabla T)^2. \tag{3.1}$$

In their theory the thermal dissipation rate is split into a plumes-plus-boundary-layers and a background components. The former can dominate for lower and the latter must dominate for higher Rayleigh numbers.

In order to check their hypothesis we define the functions $\tau(\xi)$ and $\sigma(\xi)$ according to (3.2) and evaluate the thermal dissipation rates ϵ_θ from the DNS data. The function $\tau(\xi)$ describes the percentage of the fluid volume for which the thermal dissipation rate does not exceed $\xi \times 100\,\%$ of its maximum value $\epsilon_{\theta,\max} = \max_V \epsilon_\theta$. The function $\sigma(\xi)$ describes the contribution to the volume-averaged thermal dissipation rate from those parts of the domain where ϵ_θ does not exceed $\xi \times 100\,\%$ of its maximum. Namely,

$$\tau(\xi) = \langle \delta(\xi) \rangle_V, \qquad \sigma(\xi) = \frac{\langle \delta(\xi) \epsilon_\theta \rangle_V}{\langle \epsilon_\theta \rangle_V}, \tag{3.2}$$

where $\delta(\xi)$ is the threshold function,

$$\delta(\xi) = 1, \text{ if } \frac{\epsilon_\theta}{\epsilon_{\theta,\max}} \leqslant \xi, \quad \text{and} \quad \delta(\xi) = 0 \quad \text{otherwise.}$$

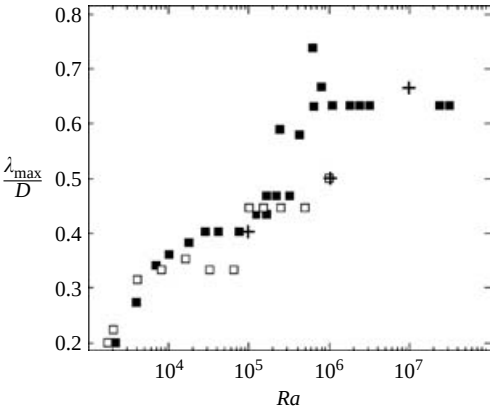

FIGURE 3. Wavelength of the maximum in the spectral distribution of lateral heat transport over Ra for $Pr = 0.7$: ■, experiments in rectangular container by Fitzjarrald (1976); □, DNS in a rectangular domain by Hartlep *et al.* (2003); and +, present DNS in the cylindrical domain.

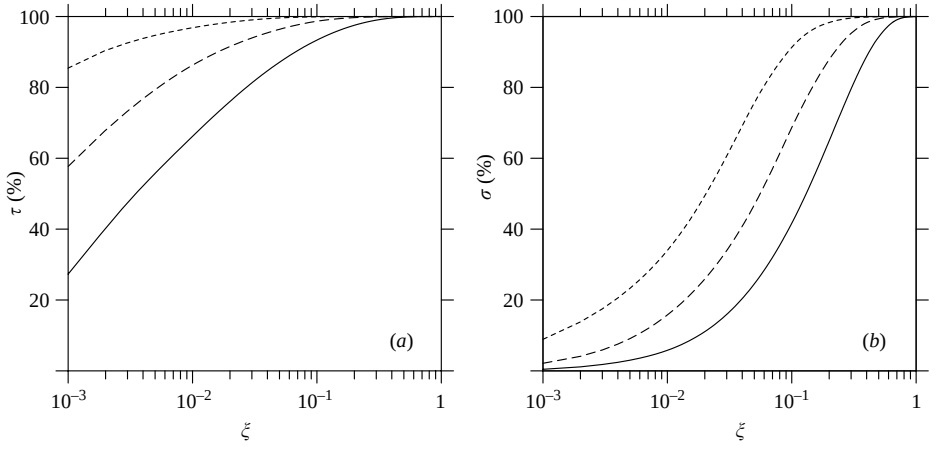

FIGURE 4. Portion of the domain, where $\epsilon_\theta(\boldsymbol{x}) \leqslant \xi\epsilon_{\theta,\max}$ (*a*) and contribution to the volume-averaged thermal dissipation rate from the parts of the domain, where $\epsilon_\theta(\boldsymbol{x}) \leqslant \xi\epsilon_{\theta,\max}$ (*b*), evaluated in the DNS for $Ra = 10^5$ (——), $Ra = 10^6$ (– – – –) and $Ra = 10^7$ (· · · · · ·).

In figure 4 $\tau(\xi)$ and $\sigma(\xi)$ are plotted as calculated from the DNS data. From figure 4(*a*) it is concluded that those parts of the domain where the thermal dissipation rate is less than 0.1 % of its maximum value (i.e. $\xi = 10^{-3}$) equals 25.3 % ($Ra = 10^5$), 57.4 % ($Ra = 10^6$) and 85.3 % ($Ra = 10^7$) of the whole domain, while figure 4(*b*) reveals that these parts contribute 0.4 % ($Ra = 10^5$), 2.1 % ($Ra = 10^6$) and 8.9 % ($Ra = 10^7$) to the volume-averaged thermal dissipation rate.

Since the turbulent background is indicated by lower values, and the plumes together with the boundary layers by higher values, of the thermal dissipation rate, there exists a value of ξ which separates these two regions. Furthermore, figure 4 reveals that the values of $\tau(\xi)$ and $\sigma(\xi)$ obtained for a certain Rayleigh number are always higher than the corresponding values for a lower Ra. Thus, the results presented above show that both the portion of the whole domain which corresponds to the turbulent background, and the background contribution to the volume-averaged thermal dissipation rate, increase with the Rayleigh number. This is true at least for the wide containers and moderate Rayleigh numbers considered and supports the

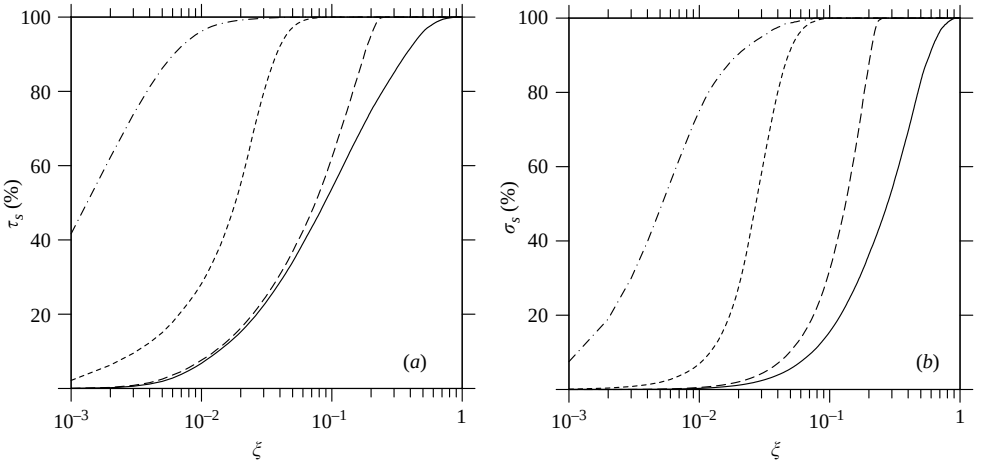

FIGURE 5. Portion of the horizontal cross-section, where $\epsilon_\theta(\boldsymbol{x}) \leqslant \xi\epsilon_{\theta,\max}$ (a) and contribution to the area-averaged thermal dissipation rate from the parts of the horizontal cross-section, where $\epsilon_\theta(\boldsymbol{x}) \leqslant \xi\epsilon_{\theta,\max}$ (b), evaluated in the DNS for $Ra = 10^5$ and different distances from the bottom, $z = 0$ (——), $z = H/(4Nu)$ (– – – –), $z = H/(2Nu)$ (· · · · · ·) and $z = 0.5H$ (– · – · –).

conjecture by Grossmann & Lohse (2004) that the background part of the thermal dissipation rate dominates for large Ra.

Further, simulating Rayleigh–Bénard convection in a slender cylindrical domain, Verzicco & Camussi (2003) observed that the contribution of the horizontal boundary layers (without plumes) to the volume-averaged thermal dissipation rate increases with Ra. As shown above, the contribution of the turbulent background also increases. Therefore we conclude that the role of the plumes in thermal convection decreases with increasing Rayleigh number.

Similarly to (3.2) we introduce the functions

$$\tau_s(\xi, z) = \langle \delta(\xi) \rangle_{S_z}, \qquad \sigma_s(\xi, z) = \frac{\langle \delta(\xi)\epsilon_\theta \rangle_{S_z}}{\langle \epsilon_\theta \rangle_{S_z}},$$

which determine the portion of the horizontal cross-section S_z and the contribution to the area-averaged thermal dissipation rate from those parts of S_z where $\epsilon_\theta(\boldsymbol{x}) \leqslant \xi\epsilon_{\theta,\max}$, for different z. In figure 5 these functions are depicted for $z = 0$, $z = H/(4Nu)$, $z = H/(2Nu)$ and $z = 0.5H$ as evaluated from the DNS for $Ra = 10^5$. One can see that near the horizontal plates the contribution of the turbulent background which corresponds to small values of ξ is negligible. On the other hand, large values of the thermal dissipation rate which correspond to large values of ξ are hardly ever reached in the bulk.

Finally we recall and derive some analytical relations, which are useful for our thermal dissipation rate analysis. Formally, a certain number of mean characteristics can be obtained by multiplication of the energy equation (2.2) with any function η and further time and volume averaging. For example, taking $\eta = z$ we calculate the mean heat transport $\langle u_z T \rangle_{t,V} = \Gamma^{-1/2} Ra^{-1/2} Pr^{-1/2}(Nu - 1)$ (see Kerr 1996), while with $\eta = T$ we obtain the mean thermal dissipation rate (see Grossmann & Lohse 2000)

$$\langle \epsilon_\theta \rangle_{t,V} = \Gamma^{1/2} Ra^{-1/2} Pr^{-1/2} Nu, \tag{3.3}$$

where $\langle \cdot \rangle_{t,V}$ denotes time and volume averaging. Taking $\eta = T^2$ we obtain $\langle C(T, \epsilon_\theta) \rangle_{t,V} = 0$, with the function $C(T, \epsilon_\theta) = T\epsilon_\theta$ used later in § 4.

A relation between the time and volume averaged $\langle \epsilon_\theta \rangle_{t,V}$ and the time and area averaged $\langle \epsilon_\theta \rangle_{t,S}$ thermal dissipation rates, where S denotes the surface of the top or the bottom plate, can be obtained using the Cauchy–Bunyakovsky–Schwarz inequality $\langle f_1 f_2 \rangle_S^2 \leqslant \langle f_1^2 \rangle_S \langle f_2^2 \rangle_S$ which holds for any functions f_1, $f_2 \in L_2(S)$. Here $L_2(S)$ is the space of functions which are square integrable on S. Taking $f_1 = \nabla T$ and $f_2 = 1$ we find $\langle \nabla T \rangle_{t,S}^2 \leqslant \langle (\nabla T)^2 \rangle_{t,S}$. This inequality together with the definition of the Nusselt number (2.3) leads to $\Gamma^2 Nu^2 \leqslant \langle (\nabla T)^2 \rangle_{t,S}$. On the other hand, combining (3.3) with (3.1) we get $\langle (\nabla T)^2 \rangle_{t,V} = \Gamma^2 Nu$.

From the last two relations the inequality

$$Nu \leqslant \frac{\langle \epsilon_\theta \rangle_{t,S}}{\langle \epsilon_\theta \rangle_{t,V}} \tag{3.4}$$

follows, which expresses that the top (or the bottom) area-averaged thermal dissipation rate is at least Nu times larger than the volume-averaged thermal dissipation rate for all Prandtl and Rayleigh numbers. We evaluated the function $\beta(Ra) = Nu^{-1} \langle \epsilon_\theta \rangle_{t,S} / \langle \epsilon_\theta \rangle_{t,V}$ from our DNS data and obtained $\beta(10^5) = 1.41$, $\beta(10^6) = 1.36$, $\beta(10^7) = 1.51$.

Relation (3.4) also indicates that the wall-normal mesh resolution at the bottom or top plates must be at least $\sqrt{Nu}$ times finer than in the bulk region to resolve properly the flow near the plates.

4. Plumes extraction

In order to separate visually the boundary layers, and the hot and cold plumes, all of which are indicated by large positive values of the thermal dissipation rate, we consider the function

$$C(T, \epsilon_\theta) = T \epsilon_\theta .$$

While plumes are visible in the instantaneous temperature field presented in figure 6(a) as mushroom-like structures, they look like the letter π if the snapshot of $C(T, \epsilon_\theta)$ in figure 6(b) is considered. The red π-structures indicate hot fluid that moves from the bottom to the top, and the blue inverted π-structures reflect zones of cold fluid moving in the opposite direction.

For the case $Ra = 10^5$ snapshots of $C(T, \epsilon_\theta)$ and superimposed velocity vectors are presented in figure 7 in three cross-sections. Plots (a),(b) and (c) show the cross-sections within the bottom boundary layer for $z = 0.1H$, slightly outside the bottom boundary layer for $z = 0.2H$ and in the middle for $z = 0.5H$. In figure 7(a) the velocity vectors reflect the displacement of the fluid due to the cold plumes entering the hot boundary layer. Due to the wall effect the cold fluid moves from the centres of the cold plume caps towards their borders and pushes away the hot fluid, which is channelled to form the roots of hot plumes. In the bulk region but still close to the bottom boundary layer for $z = 0.2H$ presented in figure 7(b) the fluid moves from the roots towards the stems of the hot plumes. The stems of both cold and hot plumes are generated at the intersections of the roots. Finally, the velocity vectors in the middle cross-section for $z = 0.5H$ in figure 7(c) highlight hot fluid moving through the stems towards the caps of the hot plumes. The cold and hot plumes look similar, but they settle upside down.

In figure 8 for each considered Rayleigh number we present in one graph $C(T, \epsilon_\theta)$ for $z = H - \lambda_\theta$ and $z = \lambda_\theta$, where $\lambda_\theta = H/(2Nu)$ is the thickness of the thermal boundary layer. The figure illustrates that the roots of hot and cold plumes have a tendency to intersect at right angles. Based on the above observations a structure of a hot plume and nesting of the hot and cold plumes in a wide container are sketched in

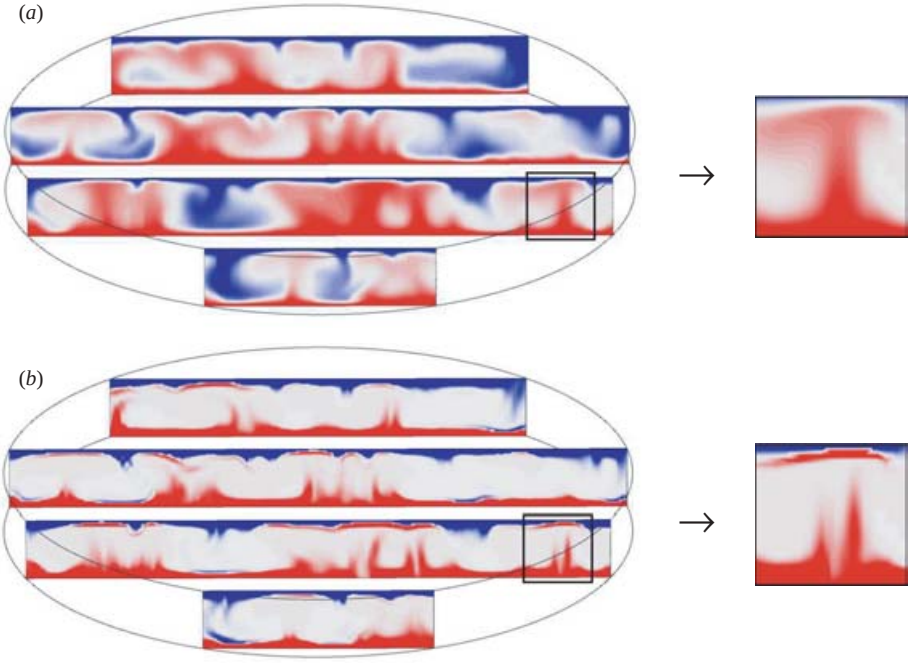

FIGURE 6. Snapshots of the temperature field T (a), $-0.5 \leqslant T \leqslant 0.5$, and of $C(T, \epsilon_\theta)$ (b), $-0.659 \leqslant C(T, \epsilon_\theta) \leqslant 0.645$, obtained in DNS for $Ra = 10^5$. Close-up views of the plumes are presented on the right. The colour scales range from blue (negative values) through white (zero) to red (positive values).

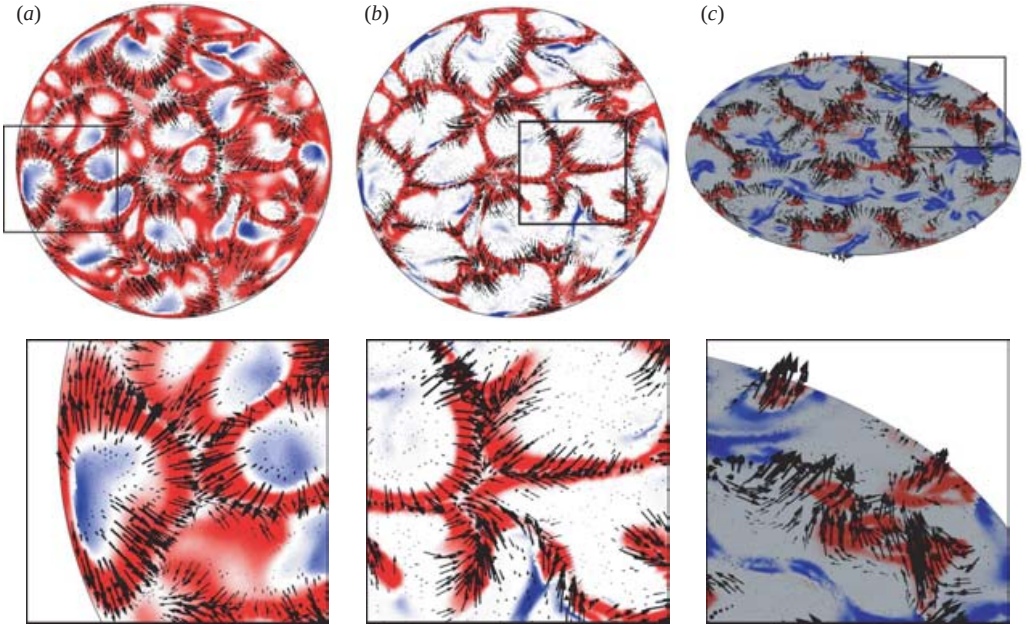

FIGURE 7. Snapshots of $C(T, \epsilon_\theta)$ in the horizontal cross-sections for $z = 0.1H$ (a), $z = 0.2H$ (b), $z = 0.5H$ (c) with superimposed velocity vectors as obtained in the DNS for $Ra = 10^5$. Close-up views are presented below. The colour scale is according to figure 6(b).

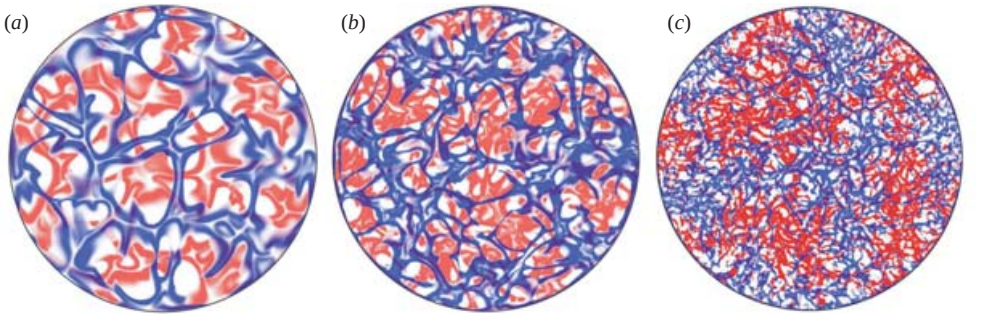

FIGURE 8. Superimposed instantaneous fields of $C(T, \epsilon_\theta)$ in horizontal cross-sections for $z = \lambda_\theta$ (red) and $z = H - \lambda_\theta$ (blue) obtained in the DNS for $Ra = 10^5$ (*a*), $Ra = 10^6$ (*b*), $Ra = 10^7$ (*c*). The colour scale is according to figure 6(*b*).

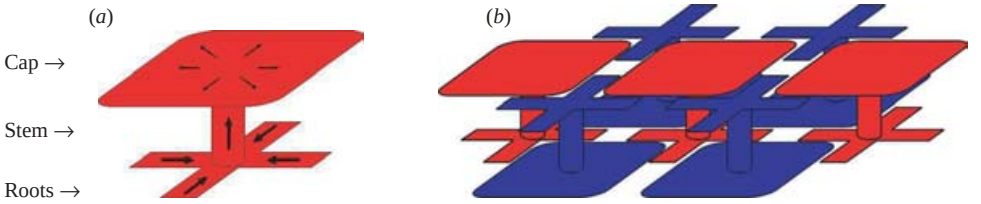

FIGURE 9. Sketch of a hot plume structure (*a*) and the formation of hot and cold plumes in wide containers (*b*) deduced from the DNS data for moderate Rayleigh numbers.

figure 9. Of course, in contrast to the sketch, plumes have a chaotic appearance, the number of roots can be different (not only four) and the shape of the plume caps is not necessarily rectangular. Further, the plumes start to cluster in certain regions of predominantly rising or descending motion if the Rayleigh number is increased from $Ra = 10^5$ to $Ra = 10^7$. The distance between these regions of clustered plumes increases and the roots of the plumes loose their tendency to intersect perpendicularly.

Generally, the analysis of the DNS data highlights the three-dimensional nature of the plumes in the moderate-Rayleigh-number regime. This distinguishes them clearly from two-dimensional rolls, l- and g-cells or spoke structures that have been observed in experiments at lower Rayleigh numbers. We also note that the large-scale structures, which Busse (1994) observed in shadowgraphs in experiments for $Ra = 2.3 \times 10^5$ and $Pr = 170$, look similar to those we obtained in the DNS for $Ra = 10^5$ and $Pr = 0.7$.

5. Conclusions

Analysing the thermal dissipation rate and its local distribution based on DNS data for Rayleigh numbers 10^5, 10^6, 10^7, $Pr = 0.7$ and $\Gamma = 10$, it was shown that the portion of the whole domain which corresponds to the turbulent background and the contribution to the volume-averaged thermal dissipation rate from the turbulent background increase with the Rayleigh number. It was further shown that plumes, which have a tendency to be arranged in a regular manner for $Ra = 10^5$, start to cluster for higher Rayleigh numbers to form a large-scale circulation. Analytically we proved that the area-averaged (over the top or the bottom plates) thermal dissipation rate is at least Nu times larger than the volume-averaged thermal dissipation rate for all Prandtl and Rayleigh numbers. Finally, analysing correlations between the temperature field and thermal dissipation rates we introduced a new way to extract plumes.

The authors are grateful to Professor André Thess for helpful discussions and to the Deutsche Forschungsgemeinschaft (DFG) for supporting this work under the contract WA 1510-1.

REFERENCES

Ahlers, G. 2005 Experiments with Rayleigh-Bénard Convection. In *Dynamics of Spatiotemporal Structures–Henri Benard Centenary Review* (ed. I. Mutabazi, E. Guyon & J. E. Wesfreid). Springer.

Ahlers, G., Grossmann, S. & Lohse, D. 2001 Hochpräzision im Kochtopf: Neues zur turbulenten Wärmekonvektion. *Physik J.* **1**, 31–37.

Assenheimer, M. & Steinberg, V. 1996 Observation of coexisting upflow and downflow hexagons in Boussinesq Rayleigh-Bénard convection. *Phys. Rev. Lett.* **76**, 756–759.

Belmonte, A. & Libchaber, A. 1996 Thermal signature of plumes in turbulent convection: The skewness of the derivative. *Phys. Rev.* E **53**, 4893–4898.

Busse, F. H. 1994 Spoke pattern convection. *Acta Mechanica Suppl.* **4**, 11–17.

Ching, E. S. C., Guo, H., Shang, X.-D., Tong, P. & Xia, K.-Q. 2004 Extraction of plumes in turbulent thermal convection. *Phys. Rev. Lett.* **93**, 124501.

Clever, R. M. & Busse, F. H. 1998 Three-dimensional knot convection in a layer heated from below. *J. Fluid Mech.* **198**, 345–363.

Fitzjarrald, D. E. 1976 An experimental study of turbulent convection in air. *J. Fluid Mech.* **73**, 693–719.

Getling, A. V. 1998 *Rayleigh-Bénard Convection.* World Scientic.

Grötzbach, G. 1983 Spatial resolution requirements for direct numerical simulation of Rayleigh-Bénard convection. *J. Comput. Phys.* **49**, 241–264.

Grossmann, S. & Lohse, D. 2000 Scaling in thermal convection: a unifying theory. *J. Fluid Mech.* **407**, 27–56.

Grossmann, S. & Lohse, D. 2004 Fluctuations in turbulent Rayleigh-Bénard convection: The role of plumes. *Phys. Fluids* **16**, 4462–4472.

Hartlep, T., Tilgner A. & Busse, F. H. 2003 Large scale structures in Rayleigh-Bénard convection at high Rayleigh numbers. *Phys. Rev. Lett.* **91**, 064501.

Juliem, K., Legg, S., McWilliams, J. & Werne, J. 1999 Plumes in rotating convection. Part 1. Ensemble statistics and dynamical balances. *J. Fluid Mech.* **391**, 151–187.

Kadanoff, L. P. 2001 Turbulent heat flow: Structures and scaling. *Phys. Today* **54**, 34–39.

Kerr, R. M. 1996 Rayleigh number scaling in numerical convection. *J. Fluid Mech.* **310**, 139–179.

Morris, S. W., Bodenschatz, E., Cannell, D. S. & Ahlers, G. 1993 Spiral defect chaos in large aspect ratio Rayleigh-Bénard convection. *Phys. Rev. Lett.* **71**, 2026–2029.

Niemela, J. J., Skrbek, L., Sreenivasan, R. R. & Donnelly, R. J. 2000 Turbulent convection at very high Rayleigh numbers. *Nature* **404**, 837–841.

Qiu, X.-L. & Tong, P. 2001 Large-scale velocity structures in turbulent thermal convection. *Phys. Rev.* E **64**, 036304.

Shishkina, O. & Wagner, C. 2004 Stability conditions for the Leapfrog-Euler scheme with central spatial discretization of any order. *J. Appl. Numer. Anal. Comput. Maths* **1**, 315–326.

Shishkina, O. & Wagner, C. 2005*a* A fourth order accurate finite volume scheme for numerical simulations of turbulent Rayleigh-Bénard convection. *C. R. Mecanique* **333**, 17–28.

Shishkina, O. & Wagner, C. 2005*b* A fourth order finite volume scheme for turbulent flow simulations in cylindrical domains. *Computers Fluids*, submitted for publication.

Siggia, E. D. 1994 High Rayleigh number convection. *Annu. Rev. Fluid Mech.* **26**, 137–168.

Verzicco, R. & Camussi, R. 2003 Numerical experiments on strongly turbulent thermal convection in a slender cylindrical cell. *J. Fluid Mech.* **477**, 19–49.

Wu, X.-Z. & Libchaber, A. 1992 Scaling relations in thermal turbulence: The aspect-ratio dependence. *Phys. Rev.* A **45**, 842–845.

Xi, H.-D., Lam, S. & Xia, K.-Q. 2004 From laminar plumes to organized flows: the onset of large-scale circulation in turbulent thermal convection. *J. Fluid Mech.* **503**, 47–56.

Zhou, S.-Q. & Xia, K.-Q. 2002 Plume statistics in thermal turbulence: mixing of an active scalar. *Phys. Rev. Lett.* **89**, 184502.